Scanning Cavity Microscopy of a Single-Crystal Diamond Membrane

Jonathan Körber[1,2,*] Maximilian Pallmann,[1] Julia Heupel,[3] Rainer Stöhr,[2] Evgenij Vasilenko,[1,4]
Thomas Hümmer,[5] Larissa Kohler,[1] Cyril Popov,[3] and David Hunger[1,4,†]

[1] *Physikalisches Institut, Karlsruhe Institute of Technology (KIT), Wolfgang-Gaede Str. 1, Karlsruhe 76131, Germany*

[2] *3rd Institute of Physics, University of Stuttgart, Pfaffenwaldring 57 Stuttgart 70569, Germany*

[3] *Institute of Nanostructure Technologies and Analytics (INA), Center for Interdisciplinary Nanostructure Science and Technology (CINSaT), University of Kassel, Heinrich-Plett-Straße 40, Kassel 34132, Germany*

[4] *Institute for Quantum Materials and Technologies (IQMT), Karlsruhe Institute of Technology (KIT), Herrmann-von-Helmholtz Platz 1, Eggenstein-Leopoldshafen 76344, Germany*

[5] *Faculty of Physics, Ludwig-Maximilians-University (LMU), Schellingstr. 4, Munich 80799, Germany*

Efficient optical interfacing of spin-bearing quantum emitters is a crucial ingredient for quantum networks. A promising route therefore is to incorporate host materials as minimally processed membranes into open-access microcavities: it enables significant emission enhancement and efficient photon collection, minimizes deteriorating influence on the quantum emitter, and allows for full spatial and spectral tunability. Here, we study the properties of a high-finesse fiber Fabry-Pérot microcavity with integrated single-crystal diamond membranes by scanning cavity microscopy. We observe the spatially resolved effects of the diamond-air interface on the cavity-mode structure: a strong correlation of the cavity finesse and mode structure with the diamond thickness and surface topography, prevalent transverse-mode mixing under diamondlike conditions, and mode-character-dependent polarization-mode splitting. Our results reveal the influence of the diamond surface on the achievable Purcell enhancement, which helps to clarify the route towards optimized spin-photon interfaces.

I. INTRODUCTION

Quantum networks built from individual optically addressable spins in solids interfaced with single photons [1,2] promise a variety of emerging applications, ranging from secure communication over large distances to distributed quantum computing, which could become the basis of a future quantum internet [3]. A key building block for this is an efficient interface between the spin and photons to enable deterministic transfer of quantum states between stationary and flying qubits [4–7]. The most powerful approach in this respect is to couple quantum emitters to optical microcavities and harness the Purcell effect to enhance the emission [8,9]. This reshapes the emission pattern into a single, well collectable mode, increases the emission fraction into the coherent zero-phonon line (ZPL), and broadens the transition due to the shortening of the excited state lifetime such that spectral fluctuations can be masked to improve photon indistinguishability.

Nitrogen-vacancy (N-V) centers in diamond are a prime candidate material system in this respect that stands out due to its exceptional spin-coherence properties, the availability of a nuclear spin quantum register [10], and lifetime-limited optical transitions that permit the generation of spin-photon entanglement [11]. Several cavity architectures have been investigated to demonstrate the basic principle of Purcell enhancement of N-V center emission [12–18]. Due to the high sensitivity of N-V centers to fluctuating electric fields, a promising approach to achieve narrow optical transitions inside a cavity is based on open-access Fabry-Pérot microcavities with incorporated minimally processed single-crystal membranes [19–24], see Fig. 1(a). This approach has led to successful experiments, both with N-V [21,24], Si-V [25,26], and Ge-V centers [27] in diamond, as well as with rare earth ions in oxide crystals [28]. However, the desired net improvement of the collection of lifetime-limited N-V center ZPL photons has not been achieved to date. In earlier work, either the collection efficiency was rather low [24], or the N-V emission linewidth was more than 2 orders of magnitude above the lifetime limit [21].

---

*jonathan.koerber@pi3.uni-stuttgart.de
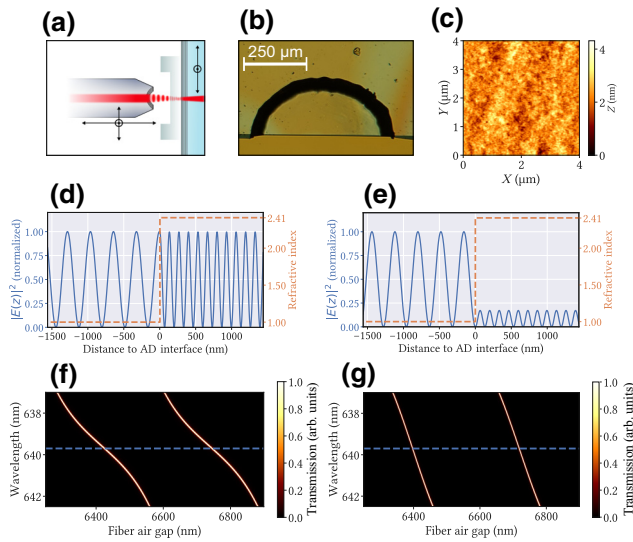†david.hunger@kit.edu

FIG. 1. (a) Schematic drawing of the cavity setup: a planar mirror (blue) carrying a diamond membrane can be moved laterally to select a region of interest. A cavity is formed together with a fiber mirror that can be nanopositioned along three axes to record raster-scanning images. (b) Microscope image of a bonded membrane. A thinned-down part for subsequent characterization lies within the region framed by the semicircle shadow. (c) AFM measurement of the membrane showing an rms roughness of $\sigma_{rms} = 0.4$ nm. Simulation of the electric field inside the cavity for a diamondlike (d) and an airlike (e) mode. The refractive-index profile (orange dashed line) highlights the air-diamond (AD) interface. (f),(g) Simulated cavity resonance frequency as a function of the mirror separation for a diamond thickness of 6035 nm (diamondlike) and 6103 nm (airlike), respectively. The probe wavelength of subsequent measurements $\lambda = 639.7$ nm is indicated by a dashed blue line.

This emphasizes the further need to understand limitations and improve the experimental realization of such systems.

In this work, we perform a systematic study of the cavity performance in the presence of diamond membranes at room temperature. We use scanning cavity microscopy [29–31] at a high finesse of up to 20 000 to probe extended areas of a membrane. We observe a spatial variation of the cavity mode character and identify spatially localized mode mixing [32,33], mostly present in diamondlike regions. We model the observed losses based on surface scattering, absorption, and mirror transmission, and find that we need to assume a larger surface roughness than measured. Additionally, we include bulk absorption in our model and find good agreement with the expected absorption for the used diamond. Furthermore, we observe an increase of the cavity loss for airlike modes with increasing diamond thickness. We suggest that the mismatch between the mode's curved phase front and the planar diamond-air interface can be the origin. Finally, we study the polarization modes of the cavity and observe an increased

polarization mode splitting with a dependence on the mode character. This reveals birefringence of the membrane, which we interpret as a signature of the local strain distribution in the material.

Our results show that mode mixing, wave-front curvature, and polarization mode splitting are key contributions to the performance of cavities with integrated membranes. We analyze how these effects depend on geometrical properties of the membrane and the cavity, providing guidance to achieve optimized spin-photon interfaces.

II. METHODS AND MATERIALS

Our experiments are performed using a fiber-based Fabry-Pérot cavity, which is schematically illustrated in Fig. 1(a). It consists of a macroscopic plane mirror and a concave mirror that is processed at the end facet of an optical fiber by CO_2-laser machining [34]. We use two different fiber tips F_A (F_B) that show concave profiles with small ellipticity, characterized by radii of curvatures (ROCs) of 33.1 (55.2) μm along one half axis and 30.5 (48.7) μm along the orthogonal one. The fiber end facets are coated by ion-beam sputtering with a distributed Bragg reflector (DBR) (Laseroptik GmbH, Garbsen, Germany), designed for a center wavelength at 637 nm. Numerical simulations using a transfer-matrix model along with the measured layer thicknesses of the DBR stacks yield transmissions of 52 (57) ppm for the fiber mirrors at a wavelength of $\lambda = 639.7$ nm that is used for the experiment. The plane mirror (M_A) consists of a superpolished fused silica substrate ($\sigma_{rms} < 0.2$ nm), coated for a transmission of 57 ppm (see the Supplemental Material [35] for details on the cavity mirrors as well as the expected and measured finesse of the assembled cavities without the presence of a diamond sample).

We study two CVD-grown single-crystal diamond samples of general grade (*Cornes Technologies, San Jose, CA, USA*) and electronic grade (*element 6*) quality. While most approaches propose the use of ultrapure, electronic grade diamond samples, also samples with a higher natural abundance of nitrogen have yielded N-V centers with very promising optical coherence properties recently [36]. Also, we choose here to study one of the two samples being nonoptimal in order to clearly identify and quantify limiting factors. Such factors can still affect optimized samples, but would be difficult to differentiate without this comparison. The main sample of this study (general grade quality) is structured using an inductively coupled plasma reactive ion etching (ICP RIE) procedure, resulting in a membrane with a minimal thickness of approximately 5 μm, as described in Ref. [23]. Characterization on 4×4 μm^2 subregions of the membrane with an atomic force microscope (AFM)—as an example shown in Fig. 1(c)—reveals a surface roughness of $\sigma_{rms} = 0.4 - 0.5$ nm after the final

etching steps. We bond the membranes onto plane mirrors via van der Waals forces. Initial interference fringes observed under a light microscope, indicating an air gap between the membrane and the mirror, broaden during the bonding procedure, and the final result for the general grade sample depicted in Fig. 1(b) shows almost no fringes (see Ref. [23] for details on the bonding procedure).

We use a custom-developed nanopositioning stage to control the cavity. It can be built cryocompatible and achieves very high passive stability and fast scanning speed [37,38]. In order to select a position on the sample, the plane mirror can be moved laterally, while the fiber can be scanned additionally along all three dimensions using piezoelectric actuators to perform the scanning cavity measurements. To probe the cavity, we couple light of a tuneable diode laser (TDL) (*Toptica DL pro 637*) at a wavelength of $\lambda = 639.7$ nm into the cavity fiber and measure the transmission behind the plane mirror using an avalanche photodiode (APD) (*Thorlabs APD130A2/M*) connected to a 12-bit digital storage oscilloscope. To obtain spatially resolved maps, we raster scan the fiber laterally on an area of about 60×60 μm^2 over the sample and modulate the cavity length at each position over multiple free spectral ranges (FSRs) at a rate of 200 Hz. The maximum transmission is recorded at each position, leading to a two-dimensional image that shows relative changes of the cavity transmission as a function of the position on the membrane, which we refer to as a cavity-transmission scan. To obtain the cavity finesse, we modulate the cavity length at a reduced rate of typically 20 Hz and probe two consecutive fundamental resonances, which we fit with Lorentzian lines. From this we calculate the finesse from the ratio of the resonance distance and the average FWHM. Due to piezo nonlinearity and hysteresis, such measurements have an uncertainty of approximately 10% unless calibrated with care. For these measurements, we align the polarization of the input light with one of the two cavity polarization modes to probe an isolated resonance.

The presence of the diamond-air interface leads to a hybridized mode structure [6,19,23,39]. Depending on the diamond thickness, the cavity standing-wave light field can either fulfill the boundary condition for the air gap part where a field node should form at the interface, called an airlike mode, or match for the mode in the diamond part where a field maximum at the interface is present, a so-called diamondlike mode, see Figs. 1(d) and 1(e). Since both conditions cannot be met simultaneously, hybridized modes form, whose dispersion, finesse, and loss strongly depend on the mode character [19,39]. For such a hybridized diamond-air cavity, the mode dispersion, i.e., the frequency-dependent shift of the cavity resonances, deviates from the linear behavior known from a bare Fabry-Pérot cavity and shows a varying slope for different diamond thickness at a fixed wavelength. As

shown in a simulation of cavity resonances in Fig. 1(f), the dispersion exhibits the smallest slope for a configuration with predominant diamondlike character, and the steepest slope for a predominant airlike configuration as in Fig. 1(g). To maximize the coupling to color centers in the membrane, diamondlike modes are beneficial because they show a larger electric field inside the diamond [39] as it can be seen by comparing Figs. 1(d) and 1(e). However, for this configuration, the scattering loss at the diamond surface becomes maximal, requiring a trade-off depending on the surface-roughness level. Furthermore, a recent study observed additional loss associated with diamondlike modes, which could not be conclusively explained by surface scattering [40]. In general, a comprehensive investigation of the cavity performance and its relation to the diamond surface topography would be desirable, while experiments to date report only punctual measurements of cavity performance on diamond membranes, mostly under airlike conditions.

III. RESULTS AND DISCUSSION

A. Mode-character-dependent cavity loss

We study the spatially varying effect of the diamond membrane on cavity modes by performing laterally resolved cavity-transmission measurements as described above. To increase the imaged area, 16 of such scans are performed at neighboring positions on the membrane with slight overlaps at the edges and consecutively stitched together.

The final transmission scan obtained with fiber mirror F_A is shown in Fig. 2 along with a height map of the membrane taken with a home-built white-light interferometric microscope (WLI). Notably, the cavity transmission in Fig. 2(b) exhibits distinct bright and dark fringes that match the shape of the height map in Fig. 2(a), evidencing the correlation between the cavity transmission and the membrane thickness. Since the composition of the cavity mode changes with the diamond thickness at a periodicity of $\lambda / (2n_d)$ [39], with $n_d = 2.41$ the refractive index of diamond, our measurements reveal the relative change of the cavity transmission as a function of the hybridized mode composition. To compare the thickness change of the diamond membrane obtained from the WLI measurement to the structure observed in cavity transmission, we estimate the region covered by the cavity scans (see Supplemental Material [35]). This region is indicated by the blue frame in Fig. 2(a). For a horizontal line at the central y position of this region, the WLI image shows a thickness change of $\Delta_h^{\text{WLI}} \approx 780$ nm. Roughly seven bright fringes along the x axis in the central y position of the cavity scan yield a thickness change of $\Delta_h^{\text{cav}} = (7-1) \times \lambda / (2n_d) \approx 800$ nm, thus showing good agreement with the WLI measurement.

To understand how the composition of the hybridized cavity mode affects the cavity losses in more detail, we
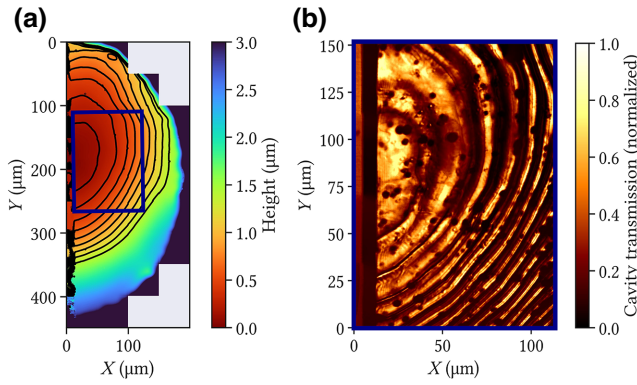
FIG. 2. (a) Surface topography of the etched diamond membrane. The blue frame indicates the region where cavity-transmission scans are performed. Black contour lines with a stepsize of 156 nm are used to highlight the height profile of the membrane. (b) Cavity-transmission map of the blue framed region in (a).

proceed with measuring the cavity finesse and the mode composition for points along a horizontal line, covering several bright and dark fringes in Fig. 3(a). As shown in Fig. 3(b), the cavity finesse spans values between 200 and 5500 and follows closely the cavity-transmission measurements. In order to link each measurement position with the character of the hybridized mode, we investigate the dispersion of the cavity mode. To this end, we couple light from a white-light laser (*Fianium Whitelase SC450*) into the cavity and measure transmission spectra with a spectrometer (*Andor Shamrock*) for different cavity lengths. The mode character is derived from the slope of the mode dispersion at the wavelength $\lambda = 639.7$ nm of the probe laser used for the finesse measurements. Here, a steep slope corresponds to a mode with high airlike character and a flat slope to a mode with high diamondlike character [19]. We define the mode character by assigning a value of 1 for the steepest slope (airlike, *A*) and 0 for the lowest slope (diamondlike, *D*) with corresponding values in between (see Supplemental Material [35]).

The results are shown together with a corresponding measurement of the finesse in Fig. 3(c). The mode character follows closely the finesse and the transmission of the cavity, proving that the losses of the cavity are dominated by effects associated with the character of the hybridized mode. To evidence the strong correlation between the cavity losses and the mode composition again over a larger region of the membrane, we scan the fiber similar to the lateral transmission measurements across the membrane and measure the finesse of the cavity at each position. The resulting finesse scan in Fig. 3(d) confirms the correlation between cavity finesse and mode composition obtained along the single line described above.

We repeat the measurement with a second fiber mirror F_B since we observed high losses for the first fiber mirror

already without diamond membrane. Taken at a slightly different position, the measurement shown in Fig. 3(e) again reflects the shape of the membrane. The finesse spans values between approximately 3000 and slightly above 20 000, which remains lower than the value observed for the cavity without membrane $\mathcal{F}_{\mathrm{max}}^{\mathrm{bare}} = 32\,400$ (see Supplemental Material [35]). To understand the contribution of different sources of loss, we analyze a line cut through the data shown in Fig. 3(e) and fit it with a model containing mode-dependent mirror transmission, scattering losses at the diamond-air interface, and absorption from the diamond [39], see Fig. 3(f). Therefore, we describe the finesse $\mathcal{F} = 2\pi/\mathcal{L}_{\mathrm{eff}}$ with the effective losses [39]

$$\mathcal{L}_{\mathrm{eff}} = \frac{E_{\mathrm{max},a}^2}{n_d E_{\mathrm{max},d}^2} \mathcal{L}^f + \mathcal{L}^m + \mathcal{L}_{\mathrm{scat}}(\sigma_{\mathrm{rms}}) + \mathcal{L}_{\mathrm{abs}}(\alpha_d).$$

Here, $\mathcal{L}^m$ ($\mathcal{L}^f$) are the losses due to transmission at the planar (fiber) mirror that we extract by a transfer-matrix model using the measured DBR-layer thicknesses from the manufacturer. The scattering loss [39]

$$\mathcal{L}_{\mathrm{scat}} = \sin^2\left(\frac{2\pi n_d t_d}{\lambda_0}\right) \times \frac{(1+n_d)(1-n_d)^2}{n_d} \times \left(\frac{4\pi \sigma_{\mathrm{rms}}}{\lambda_0}\right)^2,$$

originates from the diamond surface roughness σ_{rms}. Scattering can also occur on the diamond-mirror interface, depending on the termination of the mirror coating. Here, the mirror is terminated with a layer of high refractive index, leading to a field node at the surface such that scattering can be omitted. In addition, we include absorption loss $\mathcal{L}_{\mathrm{abs}} = 2\alpha_d t_d$ described by the absorption coefficient α_d of the diamond sample. For the general grade diamond sample, which contains an increased nitrogen concentration > 100 ppb, a broadband absorption with $\alpha_d \sim 0.1 - 0.5$ cm^{-1} is expected [41].

For all loss contributions, knowledge of the diamond thickness and the local mode character are important. Therefore, we evaluate a measurement of the cavity mode dispersion at one location, i.e., the mode frequency shift as a function of the mirror separation, and fit a simulation to the measured dispersion to obtain the thickness $t_{d,0} = 5.96$ μm. For the other locations along the line, we make use of the known mode composition change from diamondlike (*D*) to airlike (*A*) between a local finesse minimum and maximum, corresponding to a thickness change of $\lambda/(4n_d) \approx 66$ nm. We interpolate the membrane thickness along the line by a linear increase between consecutive extrema.

We then perform a fit [42] based on the described model and the interpolated thicknesses for the finesse data along the blue line in Fig. 3(e) with the surface roughness σ_{rms} and the absorption coefficient α_d as free parameters. The result is plotted in Fig. 3(f) together with the
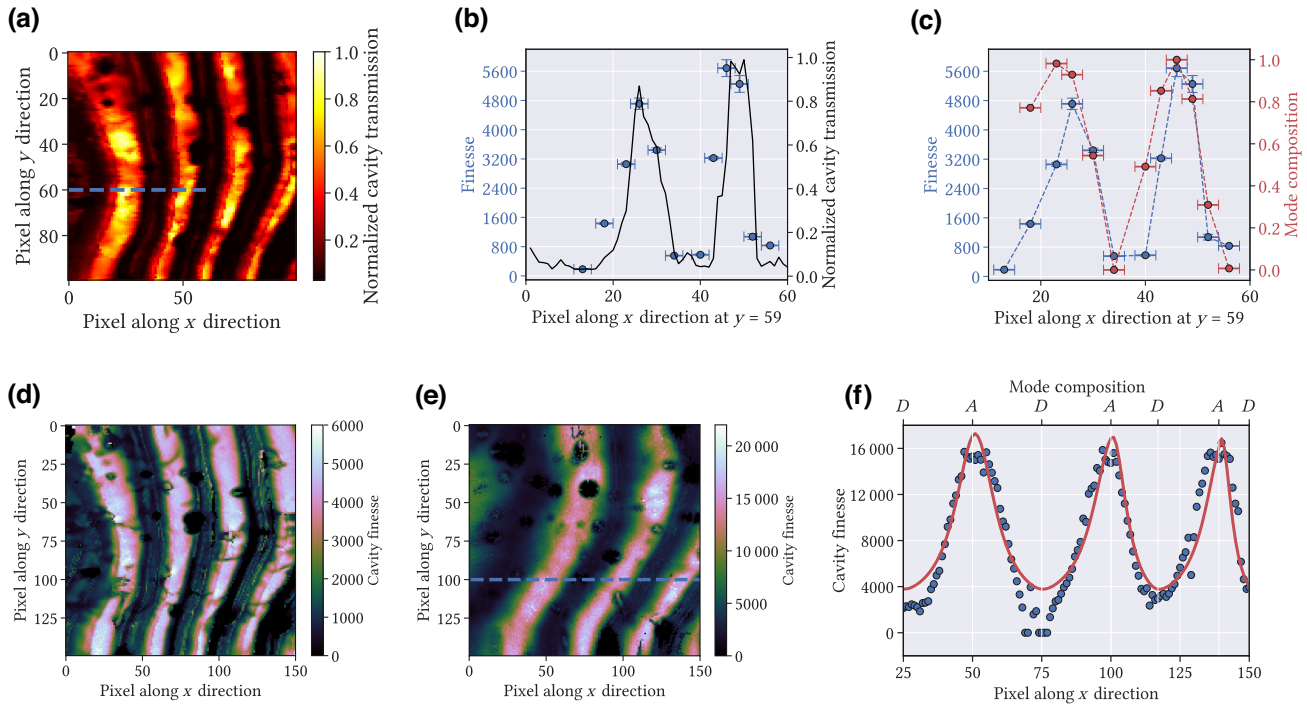
FIG. 3. (a) Cavity-transmission scan on the membrane. Each pixel shows the maximum cavity transmission from several fundamental mode orders. (b) Finesse of the cavity for points along the blue line in (a). Each data point shows the average of 50 measurements. The black curve shows the transmission data from (a). (c) Cavity finesse [data from (b)] and composition of the hybridized mode obtained by measuring the mode dispersion for each point. (d) Cavity finesse scan on the same region. (e) Cavity finesse scan using a different cavity fiber mirror achieving a higher finesse on a slightly different position on the membrane. (f) Measured cavity finesse along the dashed blue line in (e). The red line shows a fit.

measured data. We note that the deviation between fit and data around pixel 75 originates from a local defect present on the membrane, which can be seen at the respective position in Fig. 3(e). From the fit we obtain a roughness of $\sigma_{\mathrm{rms}} = (1.02 \pm 0.03)$ nm and an absorption coefficient of $\alpha_d = (0.19 \pm 0.01)$ cm^{-1}. While the absorption coefficient lies within the expected range, the predicted surface roughness is higher than the measured values of $\sigma_{\mathrm{rms}} \approx 0.4 - 0.5$ nm [23]. Therefore, we conclude that we still miss further loss contributions. Possible origins can be surface absorption due to sp^2 carbon and surface defect states, and loss originating from the mismatch between the curved cavity mode phase front and the planar membrane surface (see below). We note that by adding an antireflection coating on the membrane, one could separate loss originating from roughness and surface absorption.

B. Increased cavity losses due to transverse mode mixing

In most spatial maps of the diamond membrane, we observe sharp lines of constant mode character where the cavity finesse and transmission are significantly lower than in the surrounding. Similar but less severe behavior has been observed also for bare mirrors, and resonant

transverse-mode mixing has been identified as the origin [32,33]. It occurs when higher-order transverse modes of a neighboring longitudinal mode order $q - 1$ become resonant with a fundamental cavity mode of order q, and when boundaries such as the mirror surfaces do not match the phase fronts of Hermite-Gaussian modes, such that scattering leads to a coupling and hybridization of (near-)resonant modes. The effect is strongly dependent on the cavity length, and at large mirror separation, where low-order transverse modes fulfill the mode-mixing resonance condition, it becomes more dominant. To analyze the effect in the presence of a diamond membrane, we record transmission maps of one area [similar to Fig. 3(a)] and change the air gap of the cavity over a large range. Six different scans are shown in Fig. 4(a). As we increase the effective cavity length, we observe an overall transmission decrease as well as the sharp mode-mixing lines, which become increasingly prominent. Notably, also at shortest mirror separation, we always observe mode-mixing lines in diamondlike regions, while they only appear at large distance in airlike regions.

To see whether the overall decrease in transmission with increasing mirror separation correlates with the cavity finesse, we perform finesse scans on an airlike subregion for three different cavity lengths, see Fig. 4(b). We observe
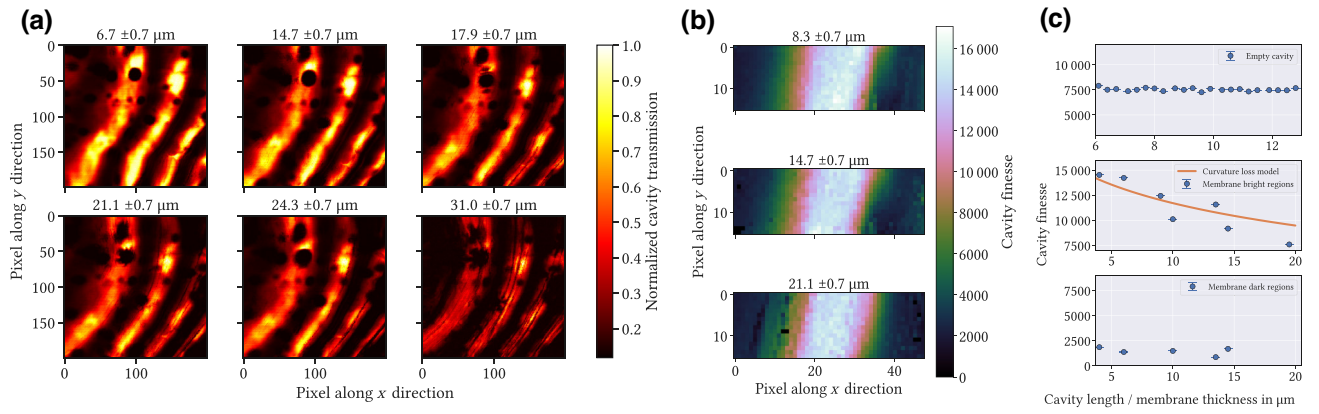
FIG. 4. (a) Cavity-transmission scans for increasing air gap and fixed membrane thickness. The effective cavity length is given above each scan. The scans are normalized to the maximum value of all scans. (b) Cavity finesse scans for different effective cavity length by changing the air gap on an airlike region. (c) Cavity finesse of the empty cavity (upper panel) for different cavity length and finesse on bright regions (central panel) and dark regions (lower panel) on the membrane for different membrane thicknesses. Each data point shows the average of at least 100 measurements and the orange curve in the central panel shows a model based on additional losses for airlike modes coming from the mode curvature at the diamond-air interface. For easier comparison, the range of shown cavity lengths in the upper panel corresponds to the effective cavity lengths resulting from the membrane thickness and the air gap of the lower two panels.

no significant drop of the maximum finesse for the different cavity lengths, and only a weak sign of mode mixing within the studied cavity length range. This indicates that the transmission drop is dominated by mode matching.

In contrast, we observe that losses under airlike conditions increase for thicker diamond membranes. To study this effect, we use a second diamond sample of electronic grade quality, which features several membranes with different thicknesses and that was bonded on a second cavity mirror M_B (see Ref. [23] for details on the sample). We perform cavity-transmission scans on regions of different thicknesses between 6 μm and 19.5 μm and measure the cavity finesse on bright (high airlike character) and dark (high diamondlike character) regions. As depicted in the central panel of Fig. 4(c), the cavity finesse on bright regions shows a strong decrease with increasing membrane thickness, dropping significantly faster than expected for bulk absorption. At the same time, we observe no drop of the cavity finesse on dark regions (diamondlike conditions) with increasing membrane thickness, shown in the lower panel of Fig. 4(c). We note that for the investigated effective cavity lengths, the empty cavity shows a stable finesse (see Fig. 4(c), upper panel), which is valid even for longer cavity lengths (for details see Supplemental Material [35]), thus ruling out effects related to the cavity fiber, i.e., clipping losses, as the origin of our observation. A plausible explanation is the shape mismatch of the diamond-air interface with the curved wave front of the cavity mode [19], which becomes more prominent with increasing membrane thickness. There, the membrane thickness approaches the Rayleigh range of the cavity mode, and the curvature of the phase front at the diamond

surface increases. Under such conditions, the cavity mode can no longer fulfill airlike conditions over the entire mode cross section, and an electric field at the interface will be present at the outer parts of the mode. This effectively reduces the airlike character of the mode and thus leads to increased scattering loss and mode mixing. As shown in the central panel of Fig. 4(c), we can model the behavior with a simple estimate where we calculate the diamond or air character based on the weighted fraction of electric field present at the diamond-air interface due to the wavefront curvature for a given cavity and membrane geometry (see Supplemental Material [35]). Since the occurrence of mode-curvature-related effects scales with the ratio of the radius of curvature of the fiber mirror to the diamond thickness rather than with just the thickness, these effects can also be relevant for experiments with thinner membranes. Consistent with this picture, we observe no significant change of the cavity finesse under diamondlike conditions for increasing membrane thickness, as the overall losses are much higher and thus the relative change smaller.

Beyond this general trend, which is present on the entire membrane and for any air gap, our measurements show that the diamond leads to significant resonant coupling between different transverse modes. To directly reveal the mode coupling, we use the cavity with fiber mirror F_B and the general grade sample to scan laterally in fine steps over a region where the transmission drops sharply and record the cavity modes at each position. We show transmission maps on three different areas where mode coupling occurs in Figs. 5(a)–5(c). To display the coupling of higher-order modes to the fundamental mode, we record cavity-transmission spectra taken by varying the cavity length,
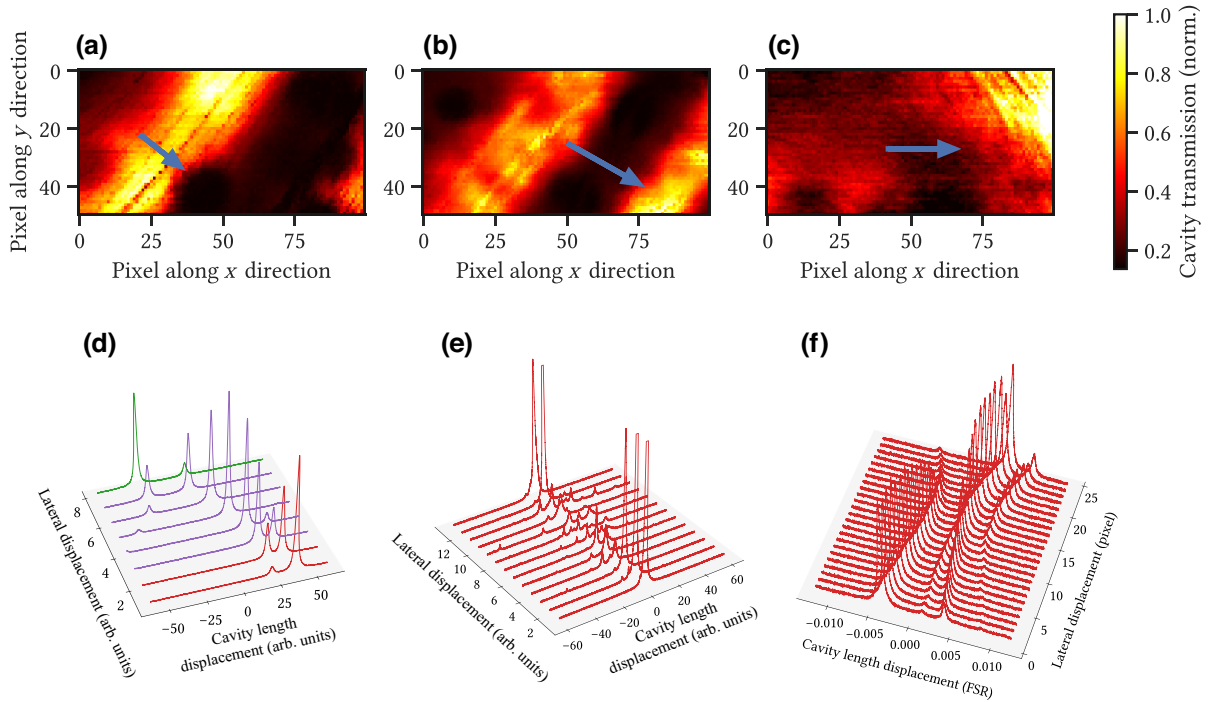
FIG. 5. (a)–(c) Cavity-transmission scans of areas with resonant mode coupling. Blue arrows indicate the location and direction of the scans shown in (d)–(f). (d) Cavity-transmission spectra under airlike conditions for positions along the blue arrow in (a). The color is changed after each avoided crossing for better visibility. (e) Transmission spectra under diamondlike conditions along the arrow shown in (b). Coupling between the fundamental mode and a series of higher-order modes leads to a strong decrease of the cavity transmission. (f) Cavity-transmission spectra for positions along the arrow shown in (c).

for each position along three different linear paths indicated in Figs. 5(a)–5(c), see Figs. 5(d)–5(f), respectively. At locations where a fundamental mode and a higher-order mode would show degeneracy, avoided crossings appear, and the transmission drops. Figure 5(d) shows the cavity spectra for a scan across an airlike region. The first spectrum (red, bottom) features one prominent fundamental mode and a second, higher-order mode approaching from the left. When both modes would become degenerate, the coupling leads to an avoided crossing. In this example, a second avoided crossing with another transverse mode and larger coupling is visible at small spatial distance.

Under diamondlike conditions, mode mixing is observed to be more severe, and it can include a large number of consecutive avoided crossings such that the transmission drops almost completely, see Fig. 5(e). Here, the laser power is increased to saturate the APD outside the avoided crossings such that the modes can still be detected while mixing. A further example with a large spatial region of mode mixing is shown in Fig. 5(f). Here, one can observe the coupling of both polarization modes. For calibration of the cavity length changes, each spectrum is recorded over more than one FSR.

The alignment of mode mixing resonance contours with the diamond membrane topography can be understood by the different effect of the membrane on the frequency of

different transverse modes [43]. Due to the larger Gouy phase of higher-order modes compared to the fundamental mode, their diamond- and airlike mode character occur for different membrane thicknesses, such that thickness variations will lead to a large variation of mode frequency differences, and transverse-mode resonance conditions will follow isocontours of constant membrane thickness.

Several contributions add to the mode mixing, such as imperfect mirror shape and misalignment of the cavity [see, e.g., Figs. 3(d) vs 3(e)], which can be both minimized. The origin of the membrane-induced mode mixing is due to imperfect surface topography such as a wedge, but also due to the shape mismatch between the planar diamond-air interface and the parabolic wave front of the cavity mode [19]. Due to this curvature, an exact airlike condition with zero field at the entire interface cannot be achieved. This introduces interface-induced mode mixing also for airlike modes. For a plano-concave cavity geometry, the wavefront curvature approaches a planar shape close to the waist on the plane mirror, such that for thin membranes, one can largely avoid diamond-induced mode mixing [25,40].

C. Polarization mode splitting and birefringence

Finally, we investigate how the diamond membrane affects the polarization modes. For cavity mirrors with broken rotational symmetry, an intrinsic polarization mode

splitting is present [44], which is also the case for the cavities used here. For the empty cavity, we measure a mode splitting of $\delta = \nu_{\text{split}}/\nu_{\text{FSR}} = 3.82 \times 10^{-5}$, which is consistent with the measured ellipticity of the concave profile of the fiber (see Supplemental Material [35]). On the diamond membrane, we observe a significantly increased and spatially varying mode splitting spanning values between $\delta = 5 \times 10^{-4}$ and 5×10^{-3}. Figure 6(a) shows a finesse scan of the investigated region of the membrane for reference of the mode character. From cavity-transmission spectra on two locations with different mode character, we find a significant difference in the polarization splitting, see Fig. 6(b). When measuring a map of the polarization splitting on the same area as shown in Fig. 6(a), we observe fringes with the same shape as for the cavity finesse, see Fig. 6(d). Positions with low finesse, i.e., diamondlike character, show a large splitting, and positions with airlike character show a smaller splitting. We suggest the mode-character-dependent energy distribution as an origin of this variation in the splitting and model it with the relative intensity in the diamond that was already used for the effective losses as

$$\delta = \frac{n_d E_{\text{max},d}^2}{E_{\text{max},a}^2} \times \delta_0.$$

A fit of this model to a line of the data from Fig. 6(d) is shown in Fig. 6(e) and yields $\delta_0 = (1.86 \pm 0.04) \times 10^{-3}$. Despite a few outliers and a nonperfect line shape, the fit confirms the mode character as a major contribution to the variation of the polarization splitting.

Even the smallest observed values for the polarization splitting within regions with high airlike character are increased compared to the empty cavity. We attribute this to birefringence of the diamond, which originates from local strain. The observed diamond-induced mode splitting in airlike regions of $\delta = 0.001$ corresponds to a refractive index difference of $\Delta n = \lambda/t_d \times \delta/2 = 5 \times 10^{-5}$, indicating an elevated local strain level.

Further, we observe a spatial variation of the intensity ratio of the polarization modes, originating from a rotation of the cavity polarization axes. To study this observation in more detail, we measure the intensity ratio of both polarization modes and calculate the corresponding polarization angle between the probe laser and one of the cavity modes by $\tan(\alpha) = E_2/E_1 = \sqrt{I_2/I_1}$, as sketched in Fig. 6(c). Here I_1 and I_2 are the transmitted intensities of the two polarization eigenmodes. As shown in Fig. 6(f), the extracted angle changes significantly over the region, showing a completely different pattern than the topography of the membrane. We ascribe this signal to the variation of the orientation of the slow axis of the birefringent diamond, which is consistent with a spatially varying strain. To exclude measurement artefacts,
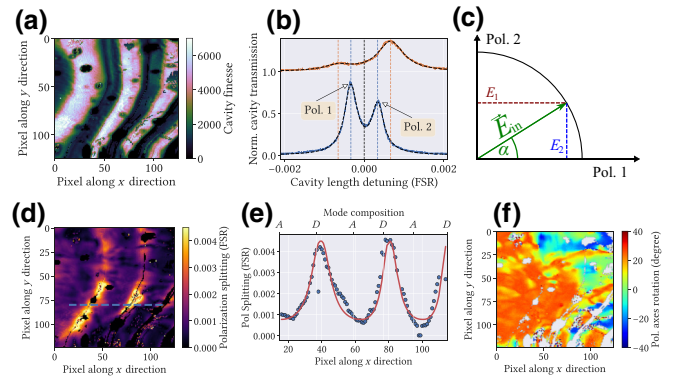

FIG. 6. Polarization splitting and rotation of the fundamental cavity modes. (a) Cavity finesse scan on the diamond membrane. (b) Fundamental cavity modes on a position with high (blue) and low (orange) finesse. The data for low finesse is shifted along the y axis for better visibility. Black dashed lines are Lorentzian fits on the transmission data. Vertical lines show the different amount of mode splitting. (c) The intensity ratio of the polarization modes can be used to determine the relative polarization angle between incoupled light and the cavity polarization modes. (d) Lateral scan of the polarization splitting in units of FSR. One finds a larger splitting for modes with higher diamondlike character. (e) Linecut along the dashed blue line in (d). The red line shows a fit. (f) Spatial map of the polarization angle obtained from the same data used for (d).

we have repeated the measurements with a second cavity with the fiber mirror F_B at a slightly shifted position (see Supplemental Material [35]), and observe the same pattern. For comparison, we also study a second electronic grade diamond sample in a cavity. There, we observe mode-character-dependent polarization splitting between $\delta = 2 \times 10^{-4}$ and 9×10^{-4}, resulting in a reduced birefringence of $\Delta n \approx 1.6 \times 10^{-5}$ (see Supplemental Material [35]). This lower level of birefringence together with the splitting induced by the ellipticity of the fiber mirror can lead to a polarization mode splitting that remains smaller than a cavity linewidth as long as the finesse remains smaller than approximately 5000. We note that we have observed also electronic grade samples with larger birefringence. This emphasizes the need to carefully select optimal samples, where 1 to 2 orders of magnitude smaller strain levels have been reported [45].

It remains an interesting question whether noticeable strain can originate from the van der Waals bond, e.g., for nonperfectly planar interfaces. This contribution could be quantified by measuring the birefringence before and after bonding. Given that the nitrogen-vacancy center in diamond is sensitive to local strain for both the optical as well as the spin levels [46,47], this might be checked in following studies by the properties of N-V centers in addition to the cavity properties. Birefringence can become a limiting factor for aligning the cavity-mode polarization with the transition dipole orientation of color centers. This

can reduce the achievable coupling strength, lead to issues with circularly polarized transitions, and limit the performance of the crossed polarization detection scheme [24]. On the other hand, suitable polarization mode splitting can be made use of for polarization-selective Purcell enhancement for efficient resonance fluorescence collection [48,49].

IV. CONCLUSIONS

In our study we use scanning cavity microscopy to evidence the effects of the topography of a diamond membrane on the cavity modes. The diamond- and airlike character strongly dominates the mode properties and cavity loss, and we are able to differentiate the different loss contributions and show the relevance of absorption loss for samples with increased nitrogen concentration. We further identify transverse mode mixing as a limiting mechanism when operating under diamondlike conditions, and increasing loss of airlike modes when the membrane thickness becomes comparable to the mirror radius of curvature. Finally, we introduce a technique to sensitively measure local birefringence and observe a mode-character-dependent polarization mode splitting. The observed loss and birefringence effects become smaller for thinner membranes, such that one can target a compromise between improved emitter coherence for thicker, and improved cavity performance for thinner membranes. Furthermore, curvature-related cavity loss at the membrane-air interface as well as mode mixing depend on the ratio between the membrane thickness and the mirror radius of curvature, suggesting an optimal choice for the radius of curvature. Our results thereby provide insight into the required cavity geometry and the properties of membranes for optimized spin-photon interfaces.

[1] D. D. Awschalom, R. Hanson, J. Wrachtrup, and B. B. Zhou, Quantum technologies with optically interfaced solid-state spins, Nat. Photon. **12**, 516 (2018).

[2] M. Atatüre, D. Englund, N. Vamivakas, S.-Y. Lee, and J. Wrachtrup, Material platforms for spin-based photonic quantum technologies, Nat. Rev. Mater. **3**, 38 (2018).

[3] S. Wehner, D. Elkouss, and R. Hanson, Quantum internet: A vision for the road ahead, Science **362**, eaam9288 (2018).

[4] S. Johnson, P. R. Dolan, and J. M. Smith, Diamond photonics for distributed quantum networks, Prog. Quantum Electron. **55**, 129 (2017).

[5] J. Borregaard, A. S. Sørensen, and P. Lodahl, Quantum networks with deterministic spin–photon interfaces, Adv. Quantum Technol. **2**, 1800091 (2019).

[6] E. Janitz, M. K. Bhaskar, and L. Childress, Cavity quantum electrodynamics with color centers in diamond, Optica **7**, 1232 (2020).

[7] M. Ruf, N. H. Wan, H. Choi, D. Englund, and R. Hanson, Quantum networks based on color centers in diamond, J. Appl. Phys. **130**, 070901 (2021).

[8] E. M. Purcell, H. C. Torrey, and R. V. Pound, Resonance absorption by nuclear magnetic moments in a solid, Phys. Rev. **69**, 37 (1946).

[9] A. Reiserer and G. Rempe, Cavity-based quantum networks with single atoms and optical photons, Rev. Mod. Phys. **87**, 1379 (2015).

[10] C. Bradley, J. Randall, M. Abobeih, R. Berrevoets, M. Degen, M. Bakker, M. Markham, D. Twitchen, and T. Taminiau, A Ten-Qubit Solid-State Spin Register with Quantum Memory up to One Minute, Phys. Rev. X **9**, 031045 (2019).

[11] H. Bernien, B. Hensen, W. Pfaff, G. Koolstra, M. S. Blok, L. Robledo, T. H. Taminiau, M. Markham, D. J. Twitchen, L. Childress, and R. Hanson, Heralded entanglement between solid-state qubits separated by three metres, Nature **497**, 86 (2013).

[12] A. Faraon, P. E. Barclay, C. Santori, K.-M. C. Fu, and R. G. Beausoleil, Resonant enhancement of the zero-phonon emission from a colour centre in a diamond cavity, Nat. Photon. **5**, 301 (2011).

[13] A. Faraon, C. Santori, Z. Huang, V. M. Acosta, and R. G. Beausoleil, Coupling of Nitrogen-Vacancy Centers to Photonic Crystal Cavities in Monocrystalline Diamond, Phys. Rev. Lett. **109**, 033604 (2012).

[14] B. J. M. Hausmann, B. J. Shields, Q. Quan, Y. Chu, N. P. de Leon, R. Evans, M. J. Burek, A. S. Zibrov, M. Markham, D. J. Twitchen, H. Park, M. D. Lukin, and M. Lončar, Coupling of NV centers to photonic crystal nanobeams in diamond, Nano Lett. **13**, 5791 (2013).

[15] R. Albrecht, A. Bommer, C. Deutsch, J. Reichel, and C. Becher, Coupling of a Single Nitrogen-Vacancy Center in Diamond to a Fiber-Based Microcavity, Phys. Rev. Lett. **110**, 243602 (2013).

[16] L. Li, T. Schröder, E. H. Chen, M. Walsh, I. Bayn, J. Goldstein, O. Gaathon, M. E. Trusheim, M. Lu, J. Mower, M. Cotlet, M. L. Markham, D. J. Twitchen, and D. Englund, Coherent spin control of a nanocavity-enhanced qubit in diamond, Nat. Commun. **6**, 6173 (2015).

[17] H. Kaupp, T. Hümmer, M. Mader, B. Schlederer, J. Benedikter, P. Haeusser, H.-C. Chang, H. Fedder, T. W. Hänsch, and D. Hunger, Purcell-Enhanced Single-Photon Emission from Nitrogen-Vacancy Centers Coupled to a Tunable Microcavity, Phys. Rev. Appl. **6**, 054010 (2016).

[18] P. R. Dolan, S. Adekanye, A. A. P. Trichet, S. Johnson, L. C. Flatten, Y. C. Chen, L. Weng, D. Hunger, H.-C. Chang, S. Castelletto, and J. M. Smith., Robust, tunable, and high purity triggered single photon source at room temperature using a nitrogen-vacancy defect in diamond in an open microcavity, Opt. Express **26**, 7056 (2018).

[19] E. Janitz, M. Ruf, M. Dimock, A. Bourassa, J. Sankey, and L. Childress, Fabry-Perot microcavity for diamond-based photonics, Phys. Rev. A **92**, 043844 (2015).

[20] S. Bogdanović, S. B. van Dam, C. Bonato, L. C. Coenen, A.-M. J. Zwerver, B. Hensen, M. S. Z. Liddy, T. Fink, A. Reiserer, M. Lončar, and R. Hanson, Design and low-temperature characterization of a tunable microcavity for diamond-based quantum networks, Appl. Phys. Lett. **110**, 171103 (2017).

[21] D. Riedel, I. Söllner, B. J. Shields, S. Starosielec, P. Appel, E. Neu, P. Maletinsky, and R. J. Warburton, Deterministic Enhancement of Coherent Photon Generation from a Nitrogen-Vacancy Center in Ultrapure Diamond, Phys. Rev. X **7**, 031040 (2017).

[22] M. Ruf, M. IJspeert, S. van Dam, N. de Jong, H. van den Berg, G. Evers, and R. Hanson, Optically coherent nitrogen-vacancy centers in micrometer-thin etched diamond membranes, Nano Lett. **19**, 3987 (2019). pMID: 31136192,

[23] J. Heupel, M. Pallmann, J. Körber, R. Merz, M. Kopnarski, R. Stöhr, J. P. Reithmaier, D. Hunger, and C. Popov, Fabrication and characterization of single-crystal diamond membranes for quantum photonics with tunable microcavities, Micromachines **11**, 1080 (2020).

[24] M. Ruf, M. Weaver, S. van Dam, and R. Hanson, Resonant Excitation and Purcell Enhancement of Coherent Nitrogen-Vacancy Centers Coupled to a Fabry-Perot Microcavity, Phys. Rev. Appl. **15**, 024049 (2021).

[25] S. Häußler, J. Benedikter, K. Bray, B. Regan, A. Dietrich, J. Twamley, I. Aharonovich, D. Hunger, and A. Kubanek, Diamond photonics platform based on silicon vacancy centers in a single-crystal diamond membrane and a fiber cavity, Phys. Rev. B **99**, 165310 (2019).

[26] M. Salz, Y. Herrmann, A. Nadarajah, A. Stahl, M. Hettrich, A. Stacey, S. Prawer, D. Hunger, and F. Schmidt-Kaler, Cryogenic platform for coupling color centers in diamond membranes to a fiber-based microcavity, Appl. Phys. B **126**, 131 (2020).

[27] R. Høy Jensen, E. Janitz, Y. Fontana, Y. He, O. Gobron, I. P. Radko, M. Bhaskar, R. Evans, C. D. Rodríguez Rosenblueth, L. Childress, A. Huck, and U. Lund Andersen, Cavity-Enhanced Photon Emission from a Single Germanium-Vacancy Center in a Diamond Membrane, Phys. Rev. Appl. **13**, 064016 (2020).

[28] B. Merkel, A. Ulanowski, and A. Reiserer, Coherent and Purcell-Enhanced Emission from Erbium Dopants in a Cryogenic High-*Q* Resonator, Phys. Rev. X **10**, 041025 (2020).

[29] M. Mader, J. Reichel, T. W. Hänsch, and D. Hunger, A scanning cavity microscope, Nat. Commun. **6**, 7249 (2015).

[30] H. Kelkar, D. Wang, D. Martín-Cano, B. Hoffmann, S. Christiansen, S. Götzinger, and V. Sandoghdar, Sensing Nanoparticles with a Cantilever-Based Scannable Optical Cavity of Low Finesse and Sub-λ^3 Volume, Phys. Rev. Appl. **4**, 054010 (2015).

[31] T. Hümmer, J. Noe, M. S. Hofmann, T. W. Hänsch, A. Högele, and D. Hunger, Cavity-enhanced Raman microscopy of individual carbon nanotubes, Nat. Commun. **7**, 12155 (2016).

[32] J. Benedikter, T. Hümmer, M. Mader, B. Schlederer, J. Reichel, T. W. Hänsch, and D. Hunger, Transverse-mode coupling and diffraction loss in tunable Fabry–Pérot microcavities, New J. Phys. **17**, 053051 (2015).

[33] J. Benedikter, T. Moosmayer, M. Mader, T. Hümmer, and D. Hunger, Transverse-mode coupling effects in scanning cavity microscopy, New J. Phys. **21**, 103029 (2019).

[34] D. Hunger, C. Deutsch, R. J. Barbour, R. J. Warburton, and J. Reichel, Laser micro-fabrication of concave, low-roughness features in silica, AIP Adv. **2**, 012119 (2012).

[35] See Supplemental Material at http://link.aps.org/supplemental/10.1103/PhysRevApplied.19.064057 for details on the used cavity fibers and mirrors, calibration of the nanopositioning system, evaluation of the hybridized mode composition, measurements of the rotation of the polarization axes and an estimate of the Purcell effect as well as a comment on the mode matching [50,51].

[36] L. Orphal-Kobin, K. Unterguggenberger, T. Pregnolato, N. Kemf, M. Matalla, R.-S. Unger, I. Ostermay, G. Pieplow, and T. Schröder, Optically Coherent Nitrogen-Vacancy Defect Centers in Diamond Nanostructures, Phys. Rev. X **13**, 011042 (2023).

[37] B. Casabone, C. Deshmukh, S. Liu, D. Serrano, A. Ferrier, T. Hümmer, P. Goldner, D. Hunger, and H. de Riedmatten, Dynamic control of Purcell enhanced emission of erbium ions in nanoparticles, Nat. Commun. **12**, 3570 (2021).

[38] M. Pallmann, T. Eichhorn, J. M. H. Benedikter, B. Casabone, T. Hümmer, and D. Hunger, A highly stable and fully tunable open microcavity platform at cryogenic temperatures, APL Photonics **8**, 046107 (2023).

[39] Suzanne B van Dam, Maximilian Ruf, and Ronald Hanson, Optimal design of diamond-air microcavities for quantum networks using an analytical approach, New J. Phys. **20**, 115004 (2018).

[40] S. Flågan, D. Riedel, A. Javadi, T. Jakubczyk, P. Maletinsky, and R. J. Warburton, A diamond-confined open microcavity featuring a high quality factor and a small mode volume, J. Appl. Phys. **131**, 113102 (2022).

[41] I. Friel, S. L. Geoghegan, D. J. Twitchen, and G. A. Scarsbrook, in *Optics and Photonics for Counterterrorism and Crime Fighting VI and Optical Materials in Defence Systems Technology VII*, Vol. 7838, edited by C. Lewis, D. Burgess, R. Zamboni, F. Kajzar, and E. M. Heckman (SPIE, 2010), p. 340.

[42] M. Newville, T. Stensitzki, D. B. Allen, and A. Ingargiola, LMFIT: Non-Linear Least-Square Minimization and Curve-Fitting for Python, (2014).

[43] J. C. Sankey, C. Yang, B. M. Zwickl, A. M. Jayich, and J. G. E. Harris, Strong and tunable nonlinear optomechanical coupling in a low-loss system, Nat. Phys. **6**, 707 (2010).

[44] M. Uphoff, M. Brekenfeld, G. Rempe, and S. Ritter, Frequency splitting of polarization eigenmodes in microscopic Fabry–Perot cavities, New J. Phys. **17**, 013053 (2015).

[45] I. Friel, S. Clewes, H. Dhillon, N. Perkins, D. Twitchen, and G. Scarsbrook, Control of surface and bulk crystalline quality in single crystal diamond grown by chemical vapour deposition, Diamond Relat. Mater. **18**, 808 (2009).

[46] A. Batalov, V. Jacques, F. Kaiser, P. Siyushev, P. Neumann, L. J. Rogers, R. L. McMurtrie, N. B. Manson, F. Jelezko, and J. Wrachtrup, Low Temperature Studies of the Excited-State Structure of Negatively Charged Nitrogen-Vacancy Color Centers in Diamond, Phys. Rev. Lett. **102**, 195506 (2009).

[47] P. Udvarhelyi, V. O. Shkolnikov, A. Gali, G. Burkard, and A. Pályi, Spin-strain interaction in nitrogen-vacancy centers in diamond, Phys. Rev. B **98**, 075201 (2018).

[48] H. Wang, *et al.*, Towards optimal single-photon sources from polarized microcavities, Nat. Photon. **13**, 770 (2019).

[49] N. Tomm, A. Javadi, N. O. Antoniadis, D. Najer, M. C. Löbl, A. R. Korsch, R. Schott, S. R. Valentin, A. D. Wieck, A. Ludwig, and R. J. Warburton, A bright and fast source of coherent single photons, Nat. Nanotechnol. **16**, 399 (2021).

[50] J. Benedikter, H. Kaupp, T. Hümmer, Y. Liang, A. Bommer, C. Becher, A. Krueger, J. M. Smith, T. W. Hänsch, and D. Hunger, Cavity-Enhanced Single-Photon Source Based on the Silicon-Vacancy Center in Diamond, Phys. Rev. Appl. **7**, 024031 (2017).

[51] G. K. Gulati, H. Takahashi, N. Podoliak, P. Horak, and M. Keller, Fiber cavities with integrated mode matching optics, Sci. Rep. **7**, 5556 (2017).